The final publication is available at

https://doi.org/10.1002/nme.2313

Additional Information

A recovery-type error estimator for the extended finite element method based on *singular+smooth* stress field splitting.

J.J. Ródenas[*†], O.A. Gónzalez-Estrada, J.E. Tarancón, F.J. Fuenmayor

Centro de Investigación de Tecnología de Vehículos (CITV)

Departamento de Ingeniería Mecánica y de Materiales (DIMM)

Universidad Politécnica de Valencia − Spain

SUMMARY

A new stress recovery procedure that provides accurate estimations of the discretization error for linear elastic fracture mechanic problems analyzed with the extended finite element method (XFEM) is presented. The procedure is an adaptation of the superconvergent patch recovery technique for the XFEM framework. It is based on 3 fundamental aspects: *a)* the use of a *singular + smooth* stress field decomposition technique involving the use of different recovery methods for each field: standard SPR for the smooth field, and reconstruction of the recovered singular field using the stress

_____

[*] Correspondence to: Juan José Ródenas, Departamento de Ingeniería Mecánica y de Materiales, Universidad Politécnica de Valencia, Camino de Vera s/n. 46022-Valencia (Spain)

[†] E-mail: jjrodena@mcm.upv.es

intensity factor K for the singular field; *b)* direct calculation of smoothed stresses at integration points using *conjoint polynomial* enhancement; and *c)* assembly of patches with elements intersected by the crack using different stress interpolation polynomials at each side of the crack. The method was validated by testing it on both, problems with an exact solution in mode I, mode II, and mixed mode, and on a problem without analytical solution. The results obtained showed the accuracy of the proposed error estimator.

KEY WORDS: Extended finite element method, error estimation, superconvergent patch recovery, singular stress field, linear elastic fracture mechanics.

1. INTRODUCTION

In recent years, the extended finite element method (XFEM) has emerged as a highly efficient numerical method for modelling inclusions and cracks [1,2]. The main advantage it offers over the standard FEM when solving linear elastic fracture mechanics (LEFM) problems is that it makes the finite element mesh independent of the crack geometry, which means that the mesh does not need to be modified during the crack propagation simulation process. The XFEM uses the partition of unity method [3] to model cracks, adding new degrees of freedom to introduce the discontinuity of the displacement field across the faces of the crack and to represent the asymptotic displacement field around the crack tip. Thanks to the advances made in the XFEM in recent years, the method is now considered to be a robust and highly accurate means of analyzing LEFM problems in 2D although inaccuracies still exist in 3D because of the oscillatory SIF fields along the crack fronts as is shown in [4-6]. Nonetheless, like the

FEM, the XFEM also yields results that are affected by the so-called discretization error.

The importance of error estimation in numerical analysis is widely acknowledged. There are different sources of error when modelling physical problems as mathematical models. Mathematical models, in addition, are usually solved by numerical methods, which are another source of error. Szabó and Babuška [7] suggested that the successful correlation between the experimental results of a physical problem and the numerical analysis of a mathematical model must be based on knowledge of the error committed. When correlating experimental and numerical results, the latter must be close to the true solution of the mathematical model so as to guarantee that any discrepancy with respect to experimental results can be ascribed to the setting of the mathematical model. Uncontrolled numerical errors may increase (or reduce) the errors caused by imprecise formulation of the mathematical model. In this respect, Strouboulis *et al.*[8] stated that because of the increasing importance and use of partition of unity (PUM) based generalized finite element methods, it was particularly important to develop procedures that were capable of providing accurate error estimates for these methods, mainly because they tend to use coarse discretizations.

The error assessment tools used in finite element analysis are well known and are usually classified [9,10] into two families: residual-type error estimators and recovery-based error estimators. The former, based on the ideas of Zienkiewicz and Zhu [11] and, in particular, on the superconvergent patch recovery (SPR) technique [12,13], are often preferred by practitioners because they are robust and simple to use [14,15]. Reference [16] contains an extensive review of the different proposals that have been published for improving the SPR technique.

The literature on error estimation methods for mesh based partition of unity methods, however, is very limited. Strouboulis *et al.* [17], for example, proposed an error estimator based on displacement field recovery for the generalized finite element method (GFEM) that yielded good results with *h*-adapted meshes. A later proposal included two *a posteriori* residual-type error estimators for GFEM.[8]. Very recently, Bordas *et al.* [18] and Bordas and Duflot [19] have presented a recovery-based error estimator for XFEM. This method proposes to enrich intrinsically the Moving Least Square recovery of Tabbara and Belytschko [20] to include information about the near-tip fields, and uses the diffraction method to introduce the discontinuity in the recovered fields. This method provided accurate results with effectivity indexes of the error estimator close to unity (optimal value) for 2D and 3D fracture mechanics problems. Duflot and Bordas [21] propose a global recovery technique where the recovered solution is sought in a space spanned by the near-tip strain fields obtained from differentiating the Westergaard asymptotic expansion. These authors indicate that this solves the problem of multiple tips, but requires a global minimization problem to be solved.

The aim of this paper is to present a new *a posteriori* recovery-based error estimator, specially adapted to the XFEM framework, that enables accurate evaluations of the discretization error for results obtained when the XFEM is used to solve LEFM problems. The technique proposed is based on the use of the Zienkiewicz and Zhu's error estimator [11] and a stress field recovery method which has been called SPR$_{\text{XFEM}}$ as it is an adaptation of the SPR technique to XFEM. This adaptation is based on 3 fundamental aspects:

- Singular field processing: decomposition of stresses into a singular field and a smooth field and use of a different recovery method for each of these fields, following a similar approach to that described in [22].

- Evaluation of recovered stresses: a *conjoint polynomial* enhancement [23] is used for the direct evaluation of recovered stresses at integration points.

- Assembly of patches containing elements intersected by the crack: use of different stress interpolation polynomials on each side of the crack.

The authors consider possible extension to 3D of the proposed technique is suitable and future work will be carried out on this matter.

The rest of the paper is structured as follows: Section 2 briefly describes the XFEM; Section 3 presents the Zienkiewicz and Zhu's error estimator in energy norm and the SPR stress field recovery technique that was used as a starting point for the development of the SPR_{XFEM} technique proposed in this paper and described in Section 4. Finally, Section 5 presents the numerical results obtained using the proposed method and Section 6 summarizes the most relevant conclusions.

2. THE EXTENDED FINITE ELEMENT METHOD

In LEFM, problems are characterized by the singularity that occurs at the crack tip. The following expressions show the first term of the asymptotic expansion of the solution in displacements and stresses for combined load modes I and II in 2D:

$$\begin{Bmatrix} u \\ v \end{Bmatrix} = \frac{K_{\mathrm{I}}}{2\mu}\sqrt{\frac{r}{2\pi}}\begin{Bmatrix} \cos\frac{\phi}{2}\left[\kappa-1+2\sin^2\frac{\phi}{2}\right] \\ \sin\frac{\phi}{2}\left[\kappa+1-2\cos^2\frac{\phi}{2}\right] \end{Bmatrix} + \frac{K_{\mathrm{II}}}{2\mu}\sqrt{\frac{r}{2\pi}}\begin{Bmatrix} \sin\frac{\phi}{2}\left[\kappa+1+2\cos^2\frac{\phi}{2}\right] \\ -\cos\frac{\phi}{2}\left[\kappa-1-2\sin^2\frac{\phi}{2}\right] \end{Bmatrix} \quad (1)$$

$$\begin{Bmatrix} \sigma_{sing,11} \\ \sigma_{sing,12} \\ \sigma_{sing,22} \end{Bmatrix} = \frac{K_I}{\sqrt{2\pi r}} \cos\frac{\phi}{2} \begin{Bmatrix} 1-\sin\frac{\phi}{2}\sin\frac{3\phi}{2} \\ \sin\frac{\phi}{2}\cos\frac{3\phi}{2} \\ 1+\sin\frac{\phi}{2}\sin\frac{3\phi}{2} \end{Bmatrix} + \frac{K_{II}}{\sqrt{2\pi r}} \begin{Bmatrix} -\sin\frac{\phi}{2}\left[2+\cos\frac{\phi}{2}\cos\frac{3\phi}{2}\right] \\ \cos\frac{\phi}{2}\left[1-\sin\frac{\phi}{2}\sin\frac{3\phi}{2}\right] \\ \sin\frac{\phi}{2}\cos\frac{\phi}{2}\cos\frac{3\phi}{2} \end{Bmatrix} \qquad (2)$$

where r and ϕ are the crack tip polar coordinates, K_I and K_{II} are the stress intensity factors (SIFs) for modes I and II, respectively, μ is the shear modulus, and κ is the Kolosov constant, defined in terms of the parameters of material E (Young's modulus) and ν (Poisson's ratio), according to the expressions:

$$\mu = \frac{E}{2(1+\nu)}, \qquad \kappa = \begin{cases} 3-4\nu & \text{plain strain} \\ \dfrac{3-\nu}{1+\nu} & \text{plain stress} \end{cases}$$

Laborious modelling procedures are required to solve problems of this nature using the conventional FEM as the mesh needs to explicitly reproduce the geometry of the crack. Furthermore, in order to adequately obtain the singular solution, the finite element mesh must be adapted by increasing, as appropriate, the density of the degrees of freedom around the crack tip; this logically also increases the computational cost of the analysis. Another solution is to add special elements to this area. With the XFEM, the displacement discontinuity caused by the existence of the crack is introduced by adding degrees of freedom to the nodes of the elements intersected by the crack. This avoids the need to adjust the topology of the mesh to the geometry of the crack [24,25]. Furthermore, to adequately represent the asymptotic field around the crack tip, the numerical model introduces a basis that spans the near-tip asymptotic field. The following expression is generally used to interpolate the displacements for a point of coordinates **x** accounting for the presence of a crack tip in a 2D XFEM model:

$$\mathbf{u}_h = \sum_{i \in I} N_i \mathbf{a}_i + \sum_{j \in J} N_j H(\mathbf{x}) \mathbf{b}_j + \sum_{m \in M} N_m \left(\sum_{\ell=1}^{4} F_\ell(\mathbf{x}) \mathbf{c}_m^\ell \right) \qquad (3)$$

In this equation N_i represents the shape functions associated with node i, $\mathbf{a}_i$, $\mathbf{b}_j$, and $\mathbf{c}_m$ represent the nodal degrees of freedom corresponding to the displacements (coefficients $\mathbf{b}_j$ are associated with the discontinuity functions $H(\mathbf{x})$, and coefficients $\mathbf{c}_m$ with the functions of the asymptotic field of the crack tip). In the above equation, I is the set of all the nodes in the mesh, M is the subset whose support contains the crack tip, and J is the subset whose support is intersected by the crack and not included in M (see Figure 1). The level set method (LSM) has been used to define the geometry of the crack in the finite element mesh according to the procedure described in [25]. In (3), the Heaviside function $H(\mathbf{x})$, with unitary modulus and a change of sign on the crack face, describes the displacement discontinuity if the finite element is intersected by the crack. The $F_\ell(\mathbf{x})$ functions form a basis that can be used to represent the first term of the asymptotic expansion of the displacement field at the crack tip described by (1). For the 2D case, the following functions are used [24]:

$$\{F_\ell(r,\phi)\} \equiv \sqrt{r}\left\{ \sin\frac{\phi}{2}, \cos\frac{\phi}{2}, \sin\frac{\phi}{2}\sin\phi, \cos\frac{\phi}{2}\sin\phi \right\} \qquad (4)$$
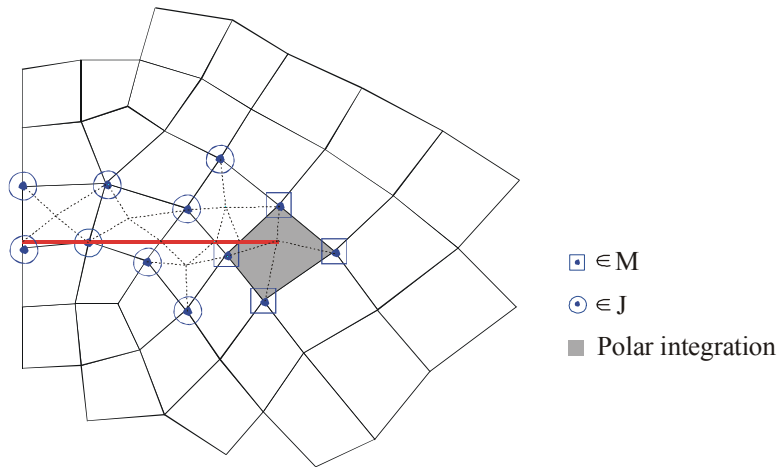

Figure 1. Classification of nodes in XFEM and definition of integration subdomains.

The methods described below have been employed in the XFEM implementation used to obtain the numerical results presented in Section 5.

2.1. Numerical integration.

A standard quadrature rule is not suitable for discontinuous functions, which is why the elements intersected by the crack are split into integration subdomains with their boundaries aligned with the crack, as in [1], in such a way that there is no discontinuity in any of the subdomains. The singularity in the crack tip elements required the use of a more accurate integration method than conventional Gaussian quadrature. In the triangular subdomains that made up these elements, the *almost polar* integration method proposed by Laborde *et al*. [26] has been used. This method consists of using the integration points of a standard quadrature of a quadrilateral transformed into a triangle (by collapsing two contiguous vertices at the singular tip). Good results were obtained using a quadrature rule of this type with 5×5 Gauss points in linear elements.

2.2. Enrichment area.

In the XFEM implementation so far described, the convergence rate of the error in energy norm is lower than the optimal convergence rate in FEM which is obtained using adaptive analysis techniques. A fixed enrichment area independent of the size h of the elements has been used to improve the convergence rate in XFEM as proposed in [26,27]. These references showed that, using this technique, h-uniform refinements in XFEM can yield the optimal convergence rate of FEM with h-adaptive refinements. One drawback to the use of the fixed enrichment area is that the condition number of the stiffness matrices increases with the number of nodes enriched with singular functions. The enrichment area was defined by a circular area $B(x_0, r_e)$ with radius r_e with its

8

centre at the crack tip x_0, see Figure 2. The subset of enriched nodes M in (3) was thus defined as the set of nodes contained in $B(x_0, r_e)$.
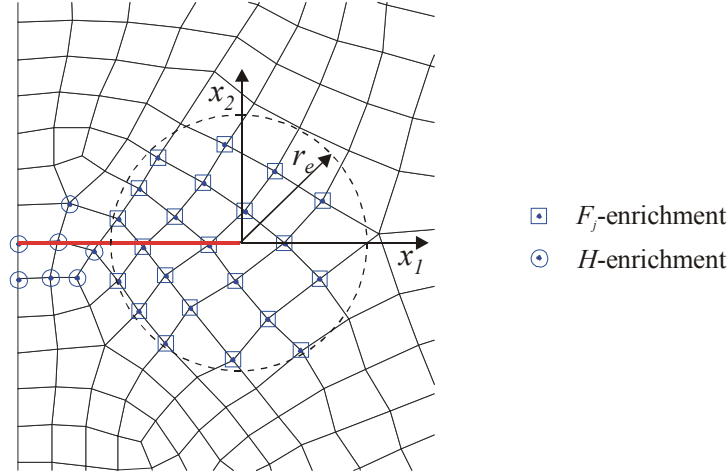

Figure 2. Enrichment using a fixed area of radius r_e.

2.3. Evaluation of stress intensity factors

SIFs are characterizing parameters in LEFM analysis. Several numerical solution post-processing methods, following local or global (energy) approaches, are commonly used to extract SIFs [28] or to calculate the energy release rate G. Local methods calculate SIFs using the solution obtained in the vicinity of the crack tip. In general terms, these methods require highly refined finite element meshes, which are often combined with singular elements. Energy methods are considered to be the most accurate and efficient methods [28,29]. Within these methods, those based on the equivalent domain integral of path independent integrals (EDI methods) are considered particularly interesting for FEM and XFEM because of their easy implementation in these frameworks.

The interaction integral [30,31] has been used in this paper to extract the SIFs. This technique provides K_{I} and K_{II} in mixed-mode problems using auxiliary fields. The interaction integral Ψ is evaluated using the following expression:

$$\Psi^{(1,2)} = \int_\Omega \left[\sigma_{ij}^{(1)} \frac{\partial u_i^{(2)}}{\partial x_1} + \sigma_{ij}^{(2)} \frac{\partial u_i^{(1)}}{\partial x_1} - W^{(1,2)} \delta_{1j} \right] \frac{\partial q}{\partial x_j} d\Omega \qquad (5)$$

In (5), the fields denoted with superscript [(1)] are the ones corresponding to the numerical approximation to the solution of the problem under analysis, while those marked with superscript [(2)] are auxiliary fields representing the asymptotic fields for modes I or II; u_i is the displacement field in direction x_i (local coordinate system at the crack tip with x_1 parallel to the crack faces, see Figure 2); $W^{(1,2)}$ stands for the strain energy in terms of the inner products $\sigma_{ij}^{(1)} \varepsilon_{ij}^{(2)} = \sigma_{ij}^{(2)} \varepsilon_{ij}^{(1)}$; δ_{1j} is the Kronecker delta and q is an arbitrary, continuous function that should be 0 at the outer boundary of the extraction domain and 1 at the crack tip. In this paper, the q function is a Plateau function with $q = 1$ for the nodes within a circle of radius r_q measured from the crack tip, and $q = 0$ for the remaining nodes. This function will also have a null value at the boundary of the problem analyzed, even if part of the boundary lies within the circle of radius r_q. Using the interaction integral, the SIFs values are obtained using the following equations:

$$K_I = E' \Psi^{(1, aux\,mode\,I)} / 2 \quad ; \quad K_{II} = E' \Psi^{(1, aux\,mode\,II)} / 2 \qquad (6)$$

where $E' = E$ in the case of plane stress and $E' = E/(1-\nu^2)$ in the case of plane strain, E being the Young's modulus and ν the Poisson's ratio.

3. ENERGY NORM ERROR ESTIMATION. THE SPR TECHNIQUE

Both FEM and XFEM analyses always have an associated discretization error that can be quantified by the energy norm error for the solution $\|\mathbf{e}\| = \|\mathbf{u} - \mathbf{u}^h\|$. In order to obtain an estimate $\|\mathbf{e}_{es}\|$ of this error in elasticity problems analyzed using the FEM, Zienkiewicz and Zhu [11] proposed the use of the ZZ estimator:

$$\|\mathbf{e}_{es}\|^2 = \int_\Omega \left(\boldsymbol{\sigma}^* - \boldsymbol{\sigma}^h\right)^T \mathbf{D}^{-1}\left(\boldsymbol{\sigma}^* - \boldsymbol{\sigma}^h\right) d\Omega \qquad (7)$$

where the domain Ω can refer to the complete domain or a local subdomain (element), $\boldsymbol{\sigma}^h$ represents the stress field provided by the FEM, $\boldsymbol{\sigma}^*$ is the so-called recovered or smoothed stress field, which is a better approximation of the exact solution than $\boldsymbol{\sigma}^h$, and $\mathbf{D}$ is the elasticity matrix that defines the stresses as $\boldsymbol{\sigma} = \mathbf{D}\boldsymbol{\varepsilon}$.

To compute the recovered stress field $\boldsymbol{\sigma}^*$ in the domain of each element, the following expression is generally used:

$$\boldsymbol{\sigma}^* = \mathbf{N}\overline{\boldsymbol{\sigma}}^* \qquad (8)$$

where $\mathbf{N}$ are the shape functions used in the interpolation of displacements and $\overline{\boldsymbol{\sigma}}^*$ contains the recovered stresses calculated at the nodes of the element. The ZZ error estimator is considered to be asymptotically exact if the recovered solution used in the error estimation is superconvergent [13].

3.1. Superconvergent Patch Recovery Technique

Zienkiewicz and Zhu further developed the SPR technique [12,13]. SPR is a superconvergent stress recovery method with a low computational cost that is widely used to calculate the nodal values of $\boldsymbol{\sigma}^*$. According to its developers, the components of $\overline{\boldsymbol{\sigma}}^*$ are obtained using a polynomial expansion, σ_p^*, of a complete order equal to that of the shape functions $\mathbf{N}$, defined over a set of contiguous elements called *patch*, which is made up of all the elements that share the same vertex node i, Figure 3.
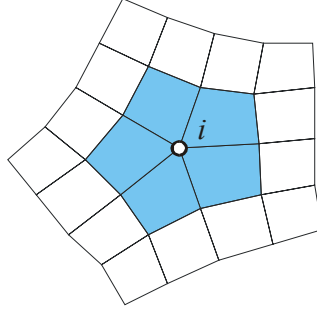
Figure 3.Element patch for node i.

For each of the stress components, σ_p^* is obtained using the following expression:

$$\sigma_p^* = \mathbf{pa} \qquad (9)$$

where $\mathbf{p}$ contains the terms of the polynomial expansion and $\mathbf{a}$ is the vector containing the unknown polynomial coefficients. For example, for one of the components of the stress vector with linear elements in the 2D case, one would have $\mathbf{p} = \{1, x, y\}$ and $\mathbf{a} = \{a_1, a_2, a_3\}^T$, where x and y are local coordinates in the cartesian reference system in which σ_p^* is expressed.

The finite element stresses calculated at the numerical integration points are used to calculate $\mathbf{a}$ using a least-squares fitting. Once these parameters have been calculated for each stress component, the values of $\overline{\boldsymbol{\sigma}}^*$ are obtained by replacing the node coordinates in the polynomial expressions $\boldsymbol{\sigma}_p^*$.

Comparative studies [15,32] have shown the technique to be robust and to yield good results in the FEM framework. Nonetheless, it has several shortcomings if used directly in XFEM to solve LEFM problems:

- Because it uses polynomials to represent recovered stresses $\boldsymbol{\sigma}^*$, the SPR technique is not suitable for describing the stress field in the vicinity of the crack tip. Related to the stress recovery techniques Boroomand and Zienkiewicz [33] indicated that

12

to overcome the difficulty associated to the representation of singularities in strains and stresses, a combination of singular functions in the radial direction and periodic functions in rotational direction could be used to evaluate smoothed values of stresses in polar coordinates. If polynomials where used to represent recovered stresses $\boldsymbol{\sigma}^*$, such a solution would be smooth and would probably be of inferior quality to the singular representation of the stress field provided by the XFEM around the crack tip. This was shown by Bordas and Duflot [18,19], who compared extended moving least squares (XMLS) recovery to standard SPR and showed that the latter led to effectivity indices that failed to converge to unity and presented very inadequate recovered solution.

▪ If there were nodes on the crack (Figure 1 shows an example where one of the Heaviside enriched nodes is exactly located on the crack), these would need to represent two different states of stress, one for each side of the discontinuity. This would require modifying the SPR technique, which normally provides just one stress state for each node.

▪ Just one set of stress interpolation polynomials σ_p^* is used for the whole patch. This method is not suitable when a patch is intersected by a crack as when this occurs it is necessary to use different functions to describe the stress fields at each side of the crack.

4. THE SPR$_{\text{XFEM}}$ TECHNIQUE

A stress recovery technique called SPR$_{\text{XFEM}}$ has been developed in order to solve the problems described above associated with the use of the SPR technique in XFEM. The proposed technique is an adaptation of the SPR technique that can be used to solve

LEFM problems with XFEM. The main differences between SPR$_{XFEM}$ and SPR are listed below:

- Direct calculation of recovered stresses at integration points: use of *conjoint polynomial* enhancement as described in [23].

- Singular field processing: splitting of stresses into singular and smooth fields.

- Assembly of patches with elements intersected by the crack: use of different stress interpolation polynomials at each side of the crack.

These modifications are described in more detail below.

4.1. Direct calculation of recovered stresses at integration points

The numerical evaluation of the integral that provides the estimated error in energy norm $\|\mathbf{e}_{es}\|$, equation (7), requires $\boldsymbol{\sigma}^*$ to be calculated at the integration points of each element. In standard SPR, these values are obtained by interpolation from nodal values $\bar{\boldsymbol{\sigma}}^*$ using (8). In other words, once the expression of the interpolation polynomials in the patch $\boldsymbol{\sigma}_p^*$ is obtained, the only values retained are those corresponding to the nodal polynomials. Blacker and Belytschko [23] proposed an improvement to the SPR technique based on the use of a *conjoint polynomial* enhancement, whereby the stresses at the integration points are directly calculated by suitably weighting the stress interpolation polynomials calculated from different patches. This reference proposes the use of the following expression to obtain $\boldsymbol{\sigma}^*$:

$$\boldsymbol{\sigma}^*(\mathbf{x}) = \sum_{i=1}^{n} N_i'(\mathbf{x}) \boldsymbol{\sigma}_{p_i}^*(\mathbf{x}) \qquad (10)$$

where $\mathbf{x}$ are the coordinates of the point at which the stresses must be evaluated, n is the number of vertex nodes of the element containing this point (only vertex nodes are used to create patches), N_i' are the shape functions of the linear version of the element (only

vertex nodes are considered), and $\boldsymbol{\sigma}_{p_i}^*$ is the vector of stress interpolation polynomials (one for each stress component) in the patch corresponding to the vertex node i.

The $\boldsymbol{\sigma}_{p_i}^*$ stresses obtained in the smoothing process are used over the entire patch domain. This contrasts with standard SPR, in which only the nodal values of the stresses calculated from each patch are retained. Note the difference between (10) and the following equation which shows the expression used to interpolate stresses using standard SPR (8) in a format similar to that used in (10):

$$\boldsymbol{\sigma}^*(\mathbf{x}) = \sum_{i=1}^{n} N_i(\mathbf{x}) \boldsymbol{\sigma}_{p_i}^*(\mathbf{x}_i) \tag{11}$$

where $\mathbf{x}_i$ is the spatial coordinate of each element node.

The use of the *conjoint polynomial* enhancement does not require the calculation of stresses at the nodes of the elements, which avoids the problems associated with having to determine two different stress states when the node is located on the crack. Remember that both the elements intersected by the crack and the elements that contain the singularity are split into integration subdomains that do not contain the crack (see Figure 1). The Gauss quadrature (integration points always inside the integration domain) has two obvious advantages. First, it ensures that the integration points are never on the crack, making it unnecessary to determine two different stress states for the same point, and second, the integration points never coincide with the crack tip, making it unnecessary to calculate stresses at the singular point.

4.2. Singular field processing

The polynomial representation of the stress field provided by the SPR technique is suitable for describing a smooth stress field but, as already mentioned, not for describing a singular solution. To solve this problem, we propose splitting the exact

stress field $\boldsymbol{\sigma}$ for a singular problem into two stress fields: a smooth field $\boldsymbol{\sigma}_{smo}$ and a

singular field $\boldsymbol{\sigma}_{sing}$:

$$\boldsymbol{\sigma} = \boldsymbol{\sigma}_{smo} + \boldsymbol{\sigma}_{sing} \tag{12}$$

Considering the above expression, the recovered stress field $\boldsymbol{\sigma}^*$ required to compute

the error estimate given in (7) can be expressed as the contribution of two recovered

stress fields, smooth $\boldsymbol{\sigma}^*_{smo}$ and singular $\boldsymbol{\sigma}^*_{sing}$:

$$\boldsymbol{\sigma}^* = \boldsymbol{\sigma}^*_{smo} + \boldsymbol{\sigma}^*_{sing} \tag{13}$$

The stress field represented by the first term of the asymptotic expansion in the

vicinity of the singular point given in (2) will be used to reconstruct the singular field

$\boldsymbol{\sigma}^*_{sing}$. Equation (2) provides an accurate representation of the singular stress field using

the SIF values, K_I and K_{II}, evaluated by means of the use of the interaction integral, see

(5) and (6).

The $\boldsymbol{\sigma}^h$ stresses directly obtained using the XFEM for this type of problems are a

finite element approximation of the field $\boldsymbol{\sigma}$. An FE-type stress representation of the

smooth field $\boldsymbol{\sigma}^h_{smo}$ can be obtained using the following equation:

$$\boldsymbol{\sigma}^h_{smo} = \boldsymbol{\sigma}^h - \boldsymbol{\sigma}_{sing} \tag{14}$$

Therefore, if it is assumed that $\boldsymbol{\sigma}^*_{sing}$ is a good approximation of $\boldsymbol{\sigma}_{sing}$, $\boldsymbol{\sigma}^h_{smo}$ can be

calculated using the following expression:

$$\boldsymbol{\sigma}^h_{smo} \approx \boldsymbol{\sigma}^h - \boldsymbol{\sigma}^*_{sing} \tag{15}$$

Once the $\boldsymbol{\sigma}^h_{smo}$ field has been obtained, an SPR-type technique can be applied to obtain

the recovered stress field $\boldsymbol{\sigma}^*_{smo}$.

This decomposition recovery technique is particularly effective in the vicinity of the singularity, although it does not need to be used in all the domain of the problem. Far from the singularity, the stress field can be adequately recovered using an SPR-type technique. In the proposed procedure, if the distance between the patch assembly node and the singularity is smaller than a radius ρ, the *singular + smooth* stress decomposition method described above is used to compute $\boldsymbol{\sigma}^*$. If the distance is greater, then an SPR-type method is used. Figure 4 illustrates how the patch stress interpolation functions $\boldsymbol{\sigma}^*_{p_i}$ are obtained in the different domain areas of the problem.
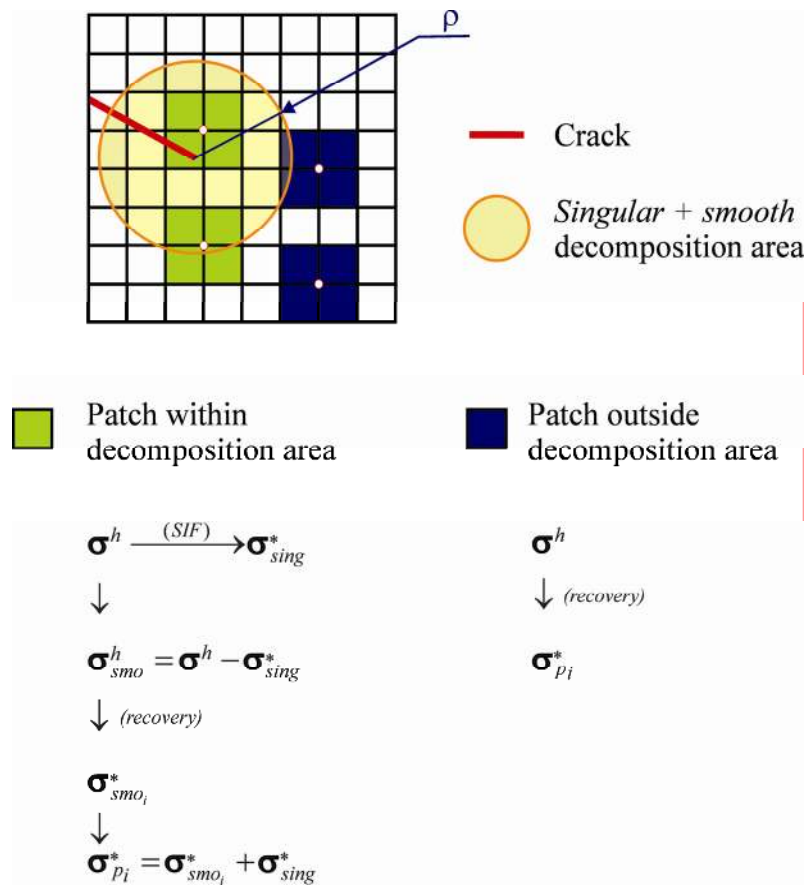
Figure 4. Calculation of $\boldsymbol{\sigma}^*_{p_i}$ in different types of patches.

17

Note that in patches outside the decomposition area, $\boldsymbol{\sigma}^*_{p_i}$ are stress interpolation polynomials, whereas in patches within the decomposition area, $\boldsymbol{\sigma}^*_{p_i}$ represent stress interpolation functions that contain a polynomial part $\boldsymbol{\sigma}^*_{smo_i}$ and a singular part $\boldsymbol{\sigma}^*_{sing}$.

It should be emphasized that the radius ρ, which defines the decomposition area (Figure 4) is, in principle, independent of the radius r_e of the enrichment area at the crack tip (Figure 2).

The stress field decomposition technique proposed in this paper was also adapted to solve singularity problems in a standard FEM framework using the procedure described in [34] as the recovery technique for the smooth stress field. Preliminary findings [22] suggest that for these type of problems, this method yields considerably improved error estimator results, both locally and globally, with respect to those obtained using standard SPR.

4.3. Assembly of patches

In XFEM, the treatment of patches in which the patch elements do not contain the crack is similar to that in FEM. When the patch contains elements that are intersected by the crack, however, the technique must be adapted.

In patches intersected by the crack, the stresses $\boldsymbol{\sigma}^*$ cannot be represented by a single set of functions $\boldsymbol{\sigma}^*_{p_i}$ at both sides of the crack because of the discontinuity of the solution introduced by the crack. In this type of patches (see Figure 5) we propose the use of different functions at each side of the crack to represent the different stress components, as is shown in the following expression:

$$
\begin{aligned}
\sigma^*_{pi} &= \mathbf{pa} = \left\{1,\, x,\, y,\, \dots \right\}\left\{a_1,\ a_2,\ a_3, \dots \right\}^T \quad \forall \mathbf{x} : H(\mathbf{x}) < 0 \\
\sigma^{*\prime}_{pi} &= \mathbf{pa'} = \left\{1,\, x,\, y,\, \dots \right\}\left\{a'_1, a'_2, a'_3, \dots \right\}^T \quad \forall \mathbf{x} : H(\mathbf{x}) > 0
\end{aligned}
\tag{16}
$$

Given that the resulting sub-patches can contain a single integration subdomain, see, for example, the upper part of patch *B* in Figure 5 (and, thus, a reduced number of integration points), it must be ensured that each subdomain contains XFEM-computed stresses at least at the same number of points as the number of terms in the polynomials used to represent the recovered stresses. Thus, if a sufficient number of Gauss points are used in the integration subdomains, the least-squares fitting used to compute the unknown vectors **a** and **a'** will always be solvable. For example, if complete 1st order polynomials were used for the stress recovery, as these polynomials have 3 unknown coefficients, at least 3 integration points should be used in each integration subdomain. Labbe and Garon [35] used this procedure in a FEM framework to overcome the difficulties associated with using SPR in patches containing few elements.
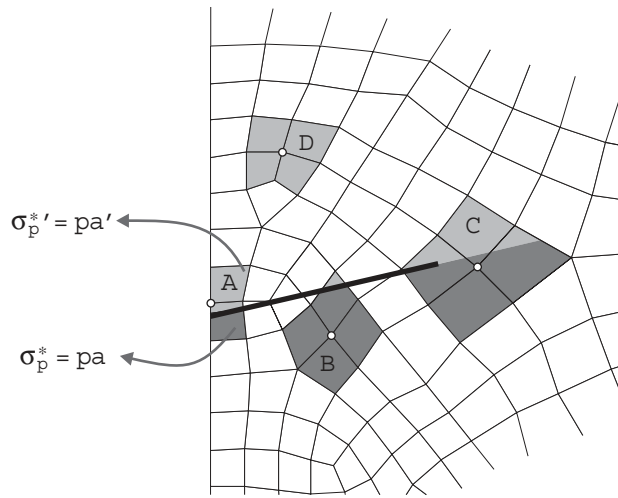
Figure 5. Patches intersected by the crack.

Two sub-patches are assembled, one on each side of the crack.

5. NUMERICAL RESULTS

The numerical analyses performed to test the behavior of the proposed technique are presented in this section. The classic Westergaard problem [36] has been used in the analyses as it is one of the few LEFM problems in mixed mode that has an exact

analytical solution. The behavior of the technique has also been tested over a problem without analytical solution.

5.1. Test problem: the Westergaard problem

The Westergaard problem consists of an infinite plate loaded with biaxial tractions $\sigma_{x\infty} = \sigma_{y\infty} = \sigma_\infty$ and τ_∞ in the infinite, with a crack of a finite length $2a$, as is shown in Figure 6. Combining the externally applied tractions one can generate stress states in pure modes I or II, or in mixed mode.
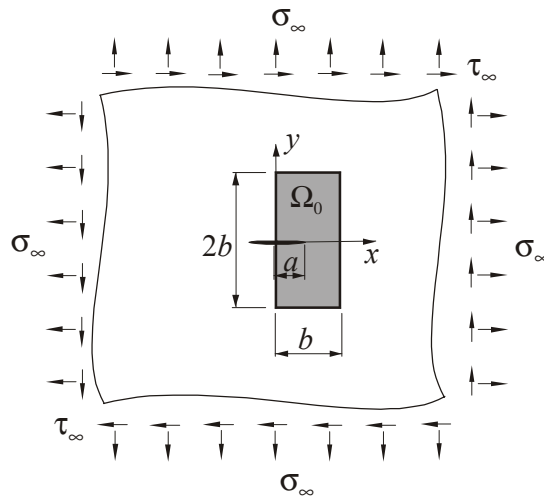
Figure 6. Westergaard problem. Infinite plate with a crack of length $2a$ subjected to uniform tractions σ_∞ (biaxial) and τ_∞. Finite portion of the domain, Ω_0, modelled with FE.

A finite portion of the domain ($a = 1$ and $b = 4$ in Figure 6) was included in the numerical model and the distribution of the stresses corresponding to the analytical Westergaard solution for modes I and II, given by the expressions below, were applied to its boundary.

$$\text{Mode I} \quad \begin{aligned} \sigma_x^I &= \frac{\sigma_\infty}{\sqrt{|t|}}\left[\left(x\cos\frac{\phi}{2}-y\sin\frac{\phi}{2}\right)+y\frac{a^2}{|t|^2}\left(m\sin\frac{\phi}{2}-n\cos\frac{\phi}{2}\right)\right] \\ \sigma_y^I &= \frac{\sigma_\infty}{\sqrt{|t|}}\left[\left(x\cos\frac{\phi}{2}-y\sin\frac{\phi}{2}\right)-y\frac{a^2}{|t|^2}\left(m\sin\frac{\phi}{2}-n\cos\frac{\phi}{2}\right)\right] \\ \tau_{xy}^I &= y\frac{a^2\sigma_\infty}{|t|^2\sqrt{|t|}}\left(m\cos\frac{\phi}{2}+n\sin\frac{\phi}{2}\right) \end{aligned} \tag{17}$$

$$\text{Mode II} \quad \begin{aligned} \sigma_x^{II} &= \frac{\tau_\infty}{\sqrt{|t|}}\left[2\left(y\cos\frac{\phi}{2}+x\sin\frac{\phi}{2}\right)-y\frac{a^2}{|t|^2}\left(m\cos\frac{\phi}{2}+n\sin\frac{\phi}{2}\right)\right] \\ \sigma_y^{II} &= y\frac{a^2\tau_\infty}{|t|^2\sqrt{|t|}}\left(m\cos\frac{\phi}{2}+n\sin\frac{\phi}{2}\right) \\ \tau_{xy}^{II} &= \frac{\tau_\infty}{\sqrt{|t|}}\left[\left(x\cos\frac{\phi}{2}-y\sin\frac{\phi}{2}\right)+y\frac{a^2}{|t|^2}\left(m\sin\frac{\phi}{2}-n\cos\frac{\phi}{2}\right)\right] \end{aligned} \tag{18}$$

In the above equations, the stress fields are expressed as a function of the coordinates x and y, whose origin is in the centre of the crack, where t, m, n and ϕ are defined as:

$$\begin{aligned} t &= z^2-a^2=(x+iy)^2-a^2=(x^2-y^2-a^2)+i(2xy)=m+in \\ m &= \text{Re}\,t=\text{Re}(z^2-a^2)=x^2-y^2-a^2 \\ n &= \text{Im}\,t=(z^2-a^2)=2xy \\ \phi &= \arg\bar{t}=\arg(m-in) \quad \text{with} \quad \phi\in\left[-\pi,\pi\right] \end{aligned} \tag{19}$$

The exact SIF values for this problem are defined as:

$$K_{I,ex}=\sigma_\infty\sqrt{\pi a} \qquad K_{II,ex}=\tau_\infty\sqrt{\pi a} \tag{20}$$

Three problems, corresponding to the *pure mode I, pure mode II,* and *mixed mode* cases of the Westergaard problem, were considered. The geometric models and boundary conditions for the mode I and mode II problems are shown in Figure 7 and Figure 8.
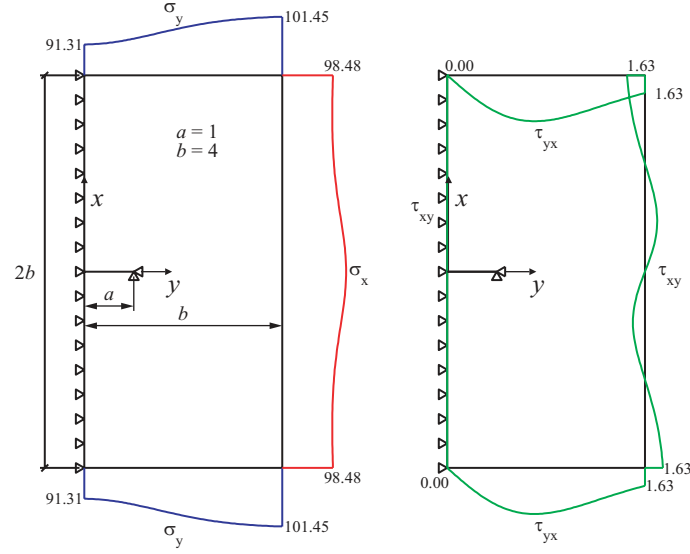
Figure 7. Mode I. Model for crack in infinite plate subjected to biaxial traction in the infinite.

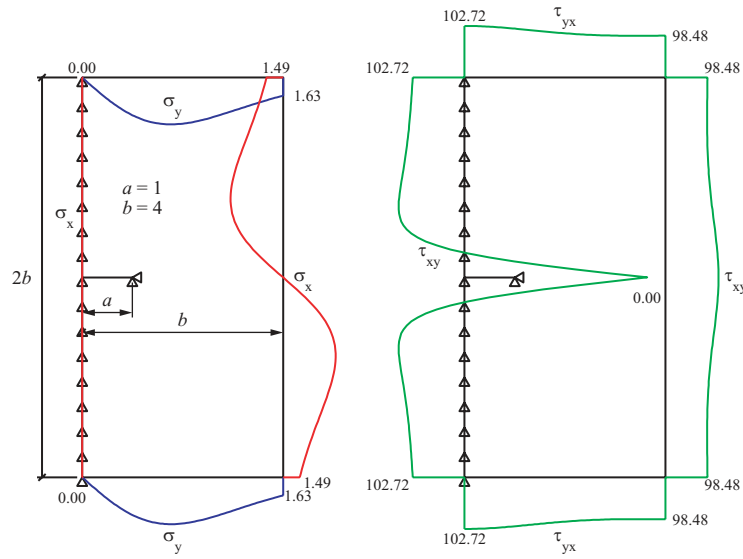($\sigma_\infty = 100$, $\tau_\infty = 0$). $K_{I,ex}$=177.2453850905516.

Figure 8. Mode II. Model for crack in infinite plate subjected to tangential stresses in the infinite.

($\sigma_\infty = 0$, $\tau_\infty = 100$). $K_{II,ex}$=177.2453850905516.

In the mixed mode problem, shown in Figure 9, the displacement of the crack tip is restricted and an antisymmetry constraint is applied to the centre of the crack (see Figure 6), so that:

$$u_A = -u_B, \quad v_A = -v_B \tag{21}$$

In the general case, this kind of constraints can be imposed, for example, using multi-point constraints involving the corresponding degrees of freedom .
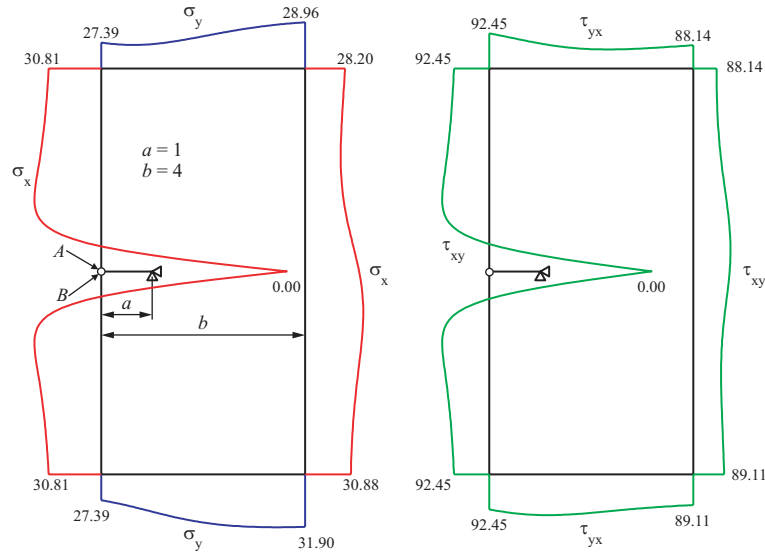
Figure 9. Mixed Mode. Model for crack in infinite plate subjected to biaxial traction in the infinite.

$(\sigma_\infty = 30, \tau_\infty = 90)$. $K_{I,ex}= 53.1736155271655$, $K_{II,ex}= 159.520846581496$.

The problems were modelled using bilinear elements with a *smooth + singular* decomposition area of a radius $\rho = 0.5$ equal to the radius r_e of the fixed enrichment area. The radius of the Plateau function for the extraction of the SIF was $r_q = 0.9$. Young's modulus was $E = 10^7$, and Poisson's ratio $\nu = 0.333$.

Following the procedure described in [34] special constraints were applied to the stress interpolation polynomials associated with boundary nodes in order to improve the accuracy of the recovered stress field at the outer boundary. The constraints considered were used to ensure that, in these nodes, the stress interpolation polynomials satisfy the equilibrium with the imposed stresses.

5.2. Effectivity index

The accuracy of the error estimator is evaluated both locally and globally. This calculation is based on the effectivity of the energy norm error estimator, which is quantified using the *effectivity index* θ:

$$\theta = \frac{\|\mathbf{e}_{es}\|}{\|\mathbf{e}\|} \tag{22}$$

The *local effectivity* parameter, *D*, is used to compute results at a local level. The definition of this parameter is based on the definition of the *robustness index* used by Babuška *et al.* [15]. For each element *e*, *D* represents the deviation from 1 (ideal value) of the estimator effectivity index in this element, θ^e, according to the following expression:

$$
\begin{aligned}
D &= \theta^e - 1 && \text{if} \quad \theta^e \geq 1 \\
D &= 1 - \frac{1}{\theta^e} && \text{if} \quad \theta^e < 1
\end{aligned}
\qquad \text{with} \quad \theta^e = \frac{\|\mathbf{e}_{es}^e\|}{\|\mathbf{e}^e\|}
\tag{23}
$$

Note that θ^e takes values in the range (0,1) when the error is underestimated and in the range (1, +∞) when it is overestimated. The definition of local effectivity given in (23) is considered appropriate given that it yields values within the interval (−∞, 0) when the error is underestimated and within (0, +∞) when it is overestimated, which allows for better comparison. Given the proposed definition, the error estimator can be considered to be of good quality if it provides *D* values close to zero.

The global effectivity index θ was used to evaluate global results. The mean value, $m(|D|)$, and the standard deviation, $\sigma(D)$, of the local effectivity were also used to evaluate the global quality of the error estimator. In an ideal scenario, where the error estimator predicts the exact error for each element in the mesh, these two values would

be zero. It can therefore be concluded that good stress field recovery methods would be those that simultaneously produce results close to zero for these two parameters.

In the global error estimator studies, the evolution of results in sequences of uniformly refined structured (Figure 10) and unstructured (Figure 11) meshes was analyzed. In the first case, the mesh sequence was defined in such a way that the crack tip always coincided with a node, this allowing to easily constraint the displacements at the crack tip as represented in Figures 7 to 9. These constraints were not applied to the unstructured mesh sequence because of the absence of a node at the crack tip. In this case a node was created on the boundary at coordinates $x = 4$ and $y = 0$. This allowed the exact analytical displacements to be imposed at that particular location.

| Mesh 1 | Mesh 2 | Mesh 3 | Mesh 4 | Mesh 5 |
| 288 elem. | 512 elem. | 800 elem. | 3200 elem. | 12800 elem. |
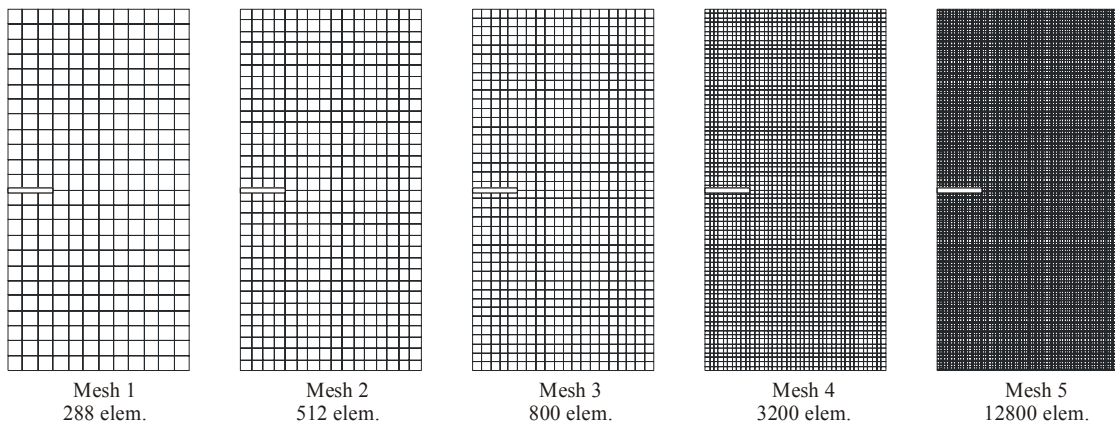
Figure 10. Sequence of structured meshes.

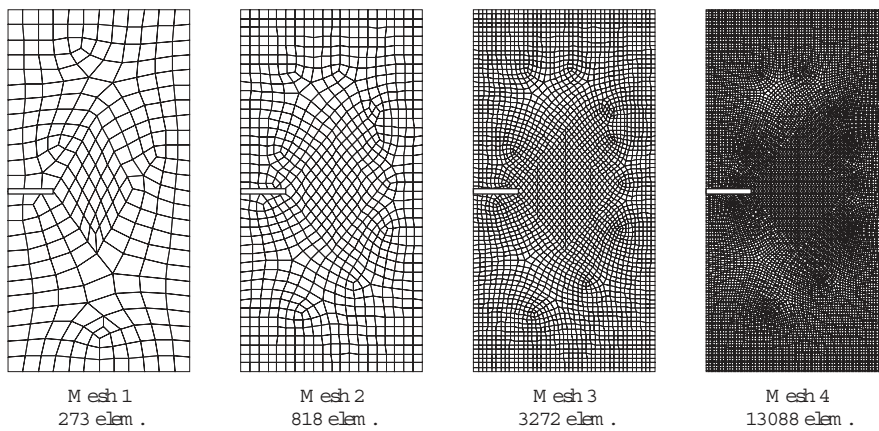| Mesh 1 | Mesh 2 | Mesh 3 | Mesh 4 |
| 273 elem. | 818 elem. | 3272 elem. | 13088 elem. |

Figure 11. Sequence of unstructured meshes.

25

Figure 12 shows the local effectivity index D for mode I, mode II, and mixed mode. These results were obtained using the third structured mesh. Figure 13 shows the results obtained in the vicinity of the singularity for an unstructured mesh of the mode I problem with element sizes similar to those used in Figure 12. Note that, in this case, the crack tip is not located over a node.

It can be seen from both figures that the error estimator is quite accurate in all the cases, with D values close to zero and always within the range $[-0.4, 0.4]$.

a. Mode I   b. Mode II   c. Mixed Mode
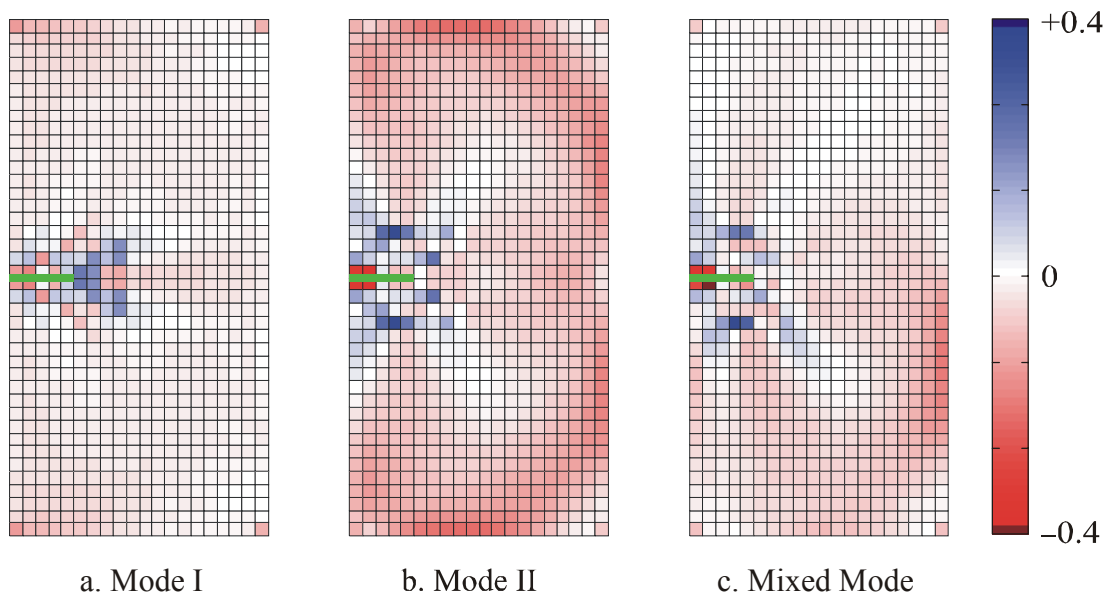
Figure 12. Local Effectivity Index D using the SPR$_{XFEM}$ technique.

Mode I, mode II, and mixed mode ($\sigma_\infty = 30$, $\tau_\infty = 90$).
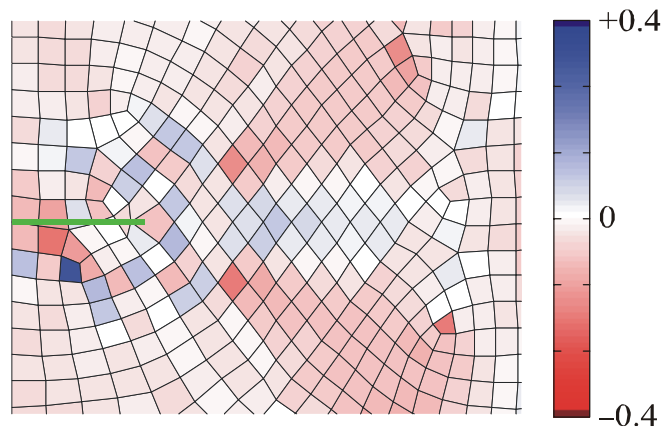
Figure 13. Local effectivity index D for Mode I in an unstructured mesh.

Figure 14 shows the evolution of θ, $m(|D|)$ and $\sigma(D)$ with respect to the number of degrees of freedom corresponding to analyses of the meshes in Figure 10. Figure 15 shows the evolution of the same parameters for the unstructured meshes shown in Figure 11. It can be seen that, in both cases, the global effectivity θ values obtained are very close to 1. The evolution of these parameters shows that less accurate results are obtained in the case of unstructured meshes, which could be due to the fact that the position of the crack tip in the element varies from mesh to mesh in unstructured meshes. This behavior has been also pointed out in reference [19], where additional scatter is present in unstructured meshes as well. Nevertheless , it should be stressed that the effectivity values are always within a very narrow band in all cases, which indicates that the error estimator is very accurate. The evolution of $m(|D|)$ and $\sigma(D)$ in these graphs show that the error estimator has performed adequately in all cases, decreasing towards zero for increasing levels of refinement.
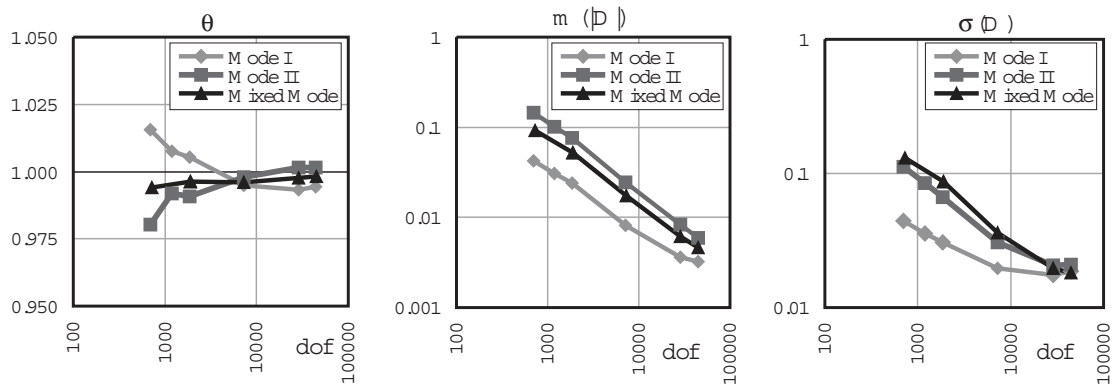

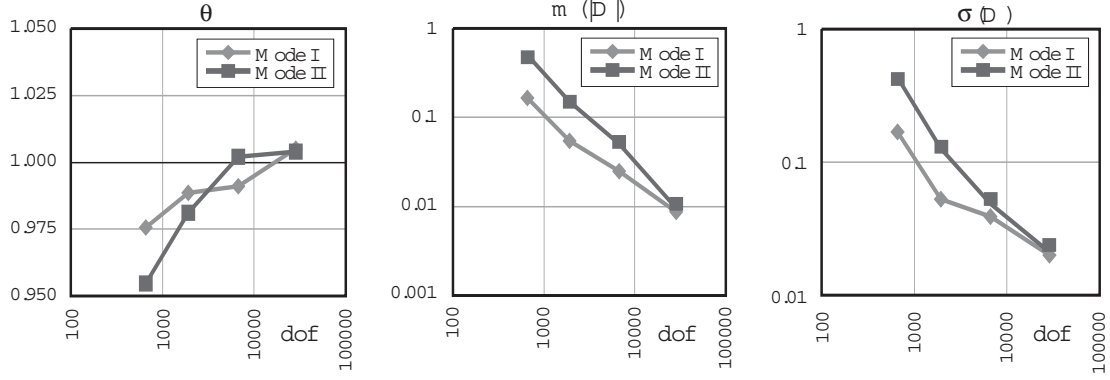Figure 14. Evolution of global indicators θ, $m(|D|)$ and $\sigma(D)$ for structured meshes.

Figure 15. Evolution of global indicators θ, $m(|D|)$ and $\sigma(D)$ for unstructured meshes for modes I and II.

5.3. Error convergence: asymptotically exact error estimator in energy norm

It is fundamental to check that the estimated error in energy norm converges to zero as the mesh size goes to zero, but also that the approximate error converges to the exact error as the mesh size tends to zero. Bordas and Duflot [18,19,21] propose the evaluation of the convergence of the estimated error as another approach to measure the quality of the estimator. The use of this approach to measure the quality of the error estimator is essential in problems where an exact solution is not available, as in these cases the effectivity of the error estimator cannot be evaluated. The optimal convergence rate of the error in energy norm as a function of the number of degrees of freedom is 0.5 in 2D problems when analyzed with linear elements and a fixed enrichment area.

Figure 16 shows the convergence of the estimated error in energy norm to zero; the convergence rates for the estimated error in energy norm for the different load modes are also indicated. In structured meshes the convergence rate achieved is approximately 0.48. In unstructured meshes convergence rates of 0.46 in Mode I and 0.50 in Mode II were obtained. These values are quite close to the optimal convergence rate of 0.5, thus proving the quality of the proposed technique.
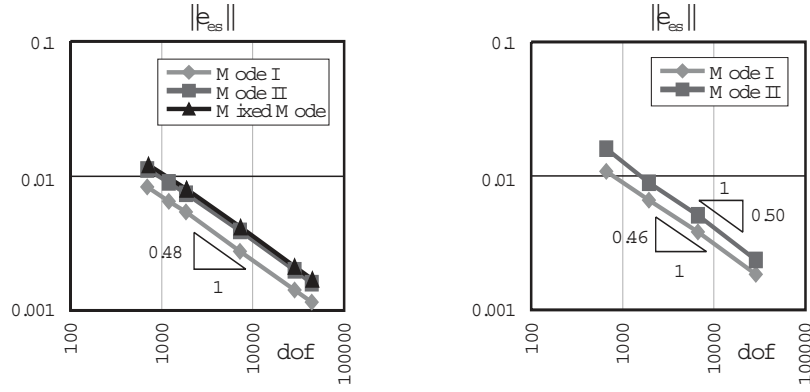
28

Figure 16. Energy norm error for structured and unstructured meshes.

When developing an error estimator one should aim to get effectivity indexes that tend to zero as the number of degrees of freedom increases, i.e. one should try to develop an asymptotically exact error estimator. Zienkiewicz and Zhu [13] proved that if the convergence rate of the error in energy norm for the recovered solution, $\|\mathbf{e}^*\| = \|\mathbf{u} - \mathbf{u}^*\|$, is higher than that for the FE solution, $\|\mathbf{e}\| = \|\mathbf{u} - \mathbf{u}^h\|$, then the error estimator will be asymptotically exact. The convergences in energy norm for $\|\mathbf{e}^*\|$ and $\|\mathbf{e}\|$ are shown in Figure 17. Two graphs are displayed in this picture. The first graph shows the error convergence curves when the whole analyzed domain is considered. The second graph shows the results obtained when the error integration area is limited to the *singular + smooth* splitting area so that the behavior of the error estimator in the vicinity of the crack tip can be analyzed in detail. It can be seen that in both cases the convergence rate for $\|\mathbf{e}^*\|$ is higher than the rate for $\|\mathbf{e}\|$. Less-uniform results when evaluating $\|\mathbf{e}^*\|$ and $\|\mathbf{e}\|$ only in the splitting area can be due to the fact that the integration area is slightly different in each of the meshes as it is only a discrete approximation to the circular enrichment area defined by r_e
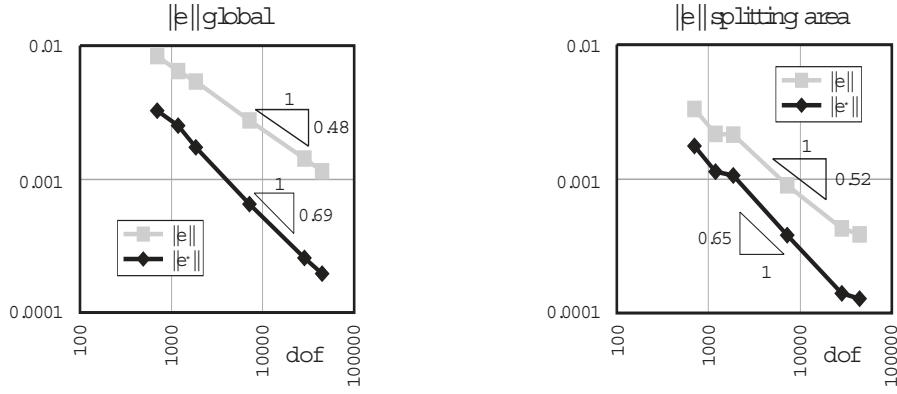
29

Figure 17. Mode I problem with structured meshes. Comparison of convergence rates for $\left\|\mathbf{e}\right\|$ and $\left\|\mathbf{e}^{*}\right\|$.

5.4. Influence of SIF accuracy

The technique described in this paper proposes the use of an interaction integral such as that indicated in (5) as it provides accurate SIF values. A series of numerical analyses were performed in order to examine how the accuracy for reasonable values of the SIFs used in the recovery of $\boldsymbol{\sigma}^{*}$ influenced the accuracy of the error estimator. The results showed that global effectivity θ is not very sensitive to the accuracy of these parameters. The accuracy of the SIFs, however, has a considerable influence on the accuracy of the estimator at the local level. Consider mesh 5 in Figure 10 subjected to load mode I as an example. In this load mode, the exact value of the SIF is $K_{I\,ex} = 177.245385090556$. To analyze the extent to which the accuracy of the SIF affected local effectivity D, this parameter was determined for $K_I = 177.215$ (value obtained on evaluating the SIF using the method proposed in this paper) and for values $K_I = 170$, $K_I = 160$ and $K_I = 150$, which would represent possible K_I values obtained using other less accurate SIF extraction methods. Figure 18 shows the local effectivity D in the vicinity of the singularity for the different K_I values considered. It can be clearly seen that the greatest degree of accuracy is achieved with the K_I value obtained using the SIF extraction method proposed in this paper. These results clearly show the

30

need to use SIF evaluation methods that provide the greatest degree of accuracy possible.
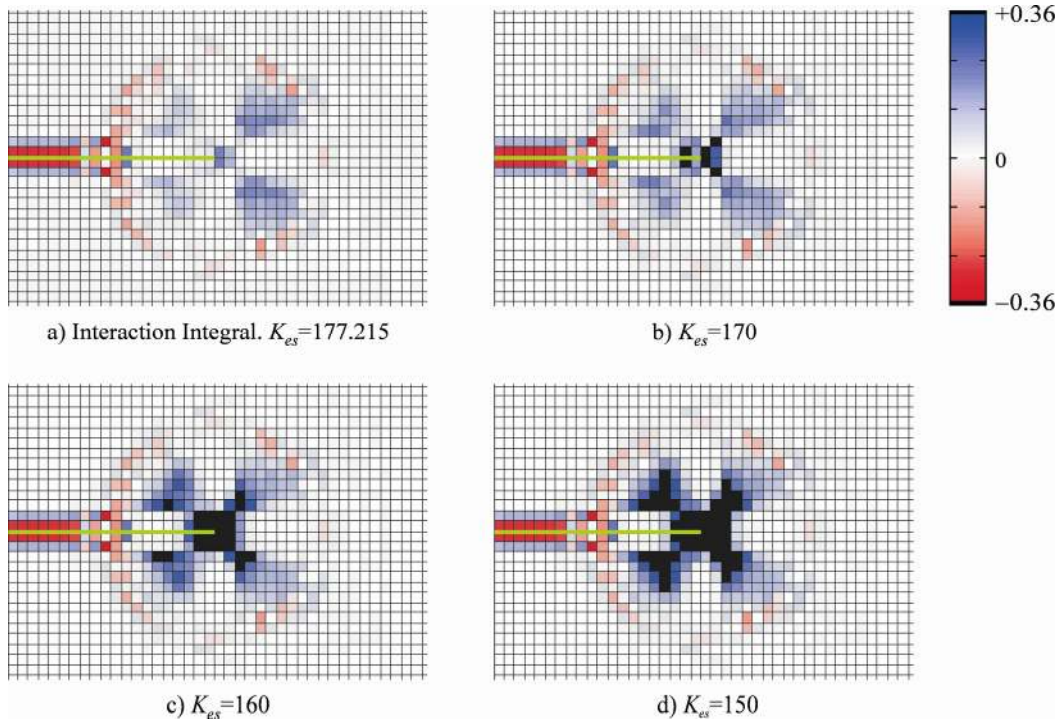

Figure 18. Mode I problem. Local effectivity index D in the vicinity of the singularity in a mesh of 12800 elements for different degrees of accuracy of K_I. ($K_{I\,exact}$= 177.245385090556).

5.5. *Effect of the singular+smooth decomposition technique.*

The aim of this section is to analyze the effect of the use of the *singular+smooth* splitting technique over the accuracy of the error estimator. Figure 19 and Figure 20 are used to compare the results obtained using the technique proposed in this paper (SPR$_{XFEM}$ curves) with those obtained when SIF = 0 is used to recover the singular field in order to avoid the *singular+smooth* splitting (SPR curves). These figures show that effectivity results corresponding to the SPR curve do not converge to unity, and that the convergence rate of the error in energy norm is only 0.26, whereas 0.48 is obtained when the *singular+smooth* splitting is used. The slope of the mean value of $|D|$ is smaller than that of the proposed technique, while the value of $\sigma(D)$ does not converge

31

to zero in the SPR curve. Hence, it can be concluded that without the *singular+smooth* splitting the recovered stress field is not sufficiently accurate and will not provide an asymptotically exact error estimator. The splitting technique is therefore necessary in the proposed method to obtain effectivity indexes that approach unity for increasing number of dof.
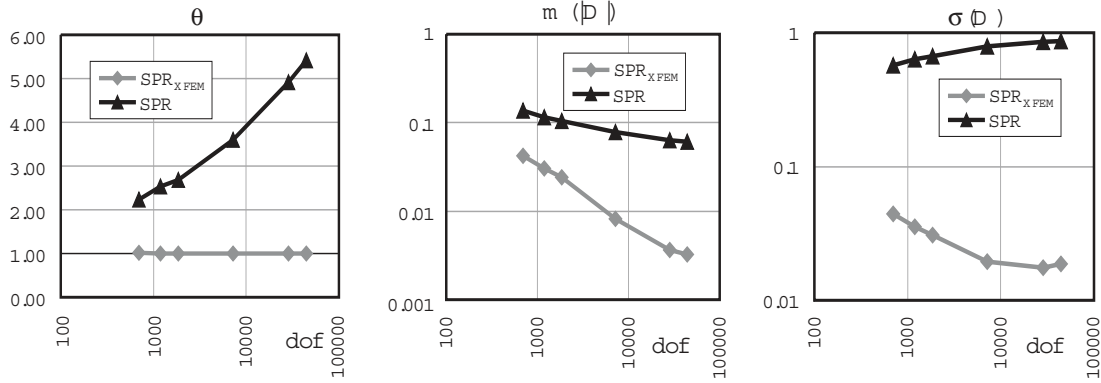

Figure 19. Mode I problem with structured meshes. Global indicators θ, $m(|D|)$ and $\sigma(D)$ with *singular+smooth* splitting (SPR$_{XFEM}$) and without it (SPR).
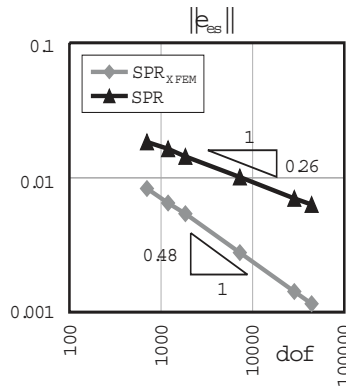

Figure 20. Mode I problem with structured meshes. Energy norm error with *singular +smooth* splitting (SPR$_{XFEM}$) and without it (SPR).

5.6. Influence of the decomposition area size

The influence of the radius ρ, which defines the decomposition area, using a fixed enrichment radius $r_e = 0.5$ is studied in this section. The results obtained with several radii ρ inside and outside the enrichment area are plotted in Figure 21 and Figure 22.
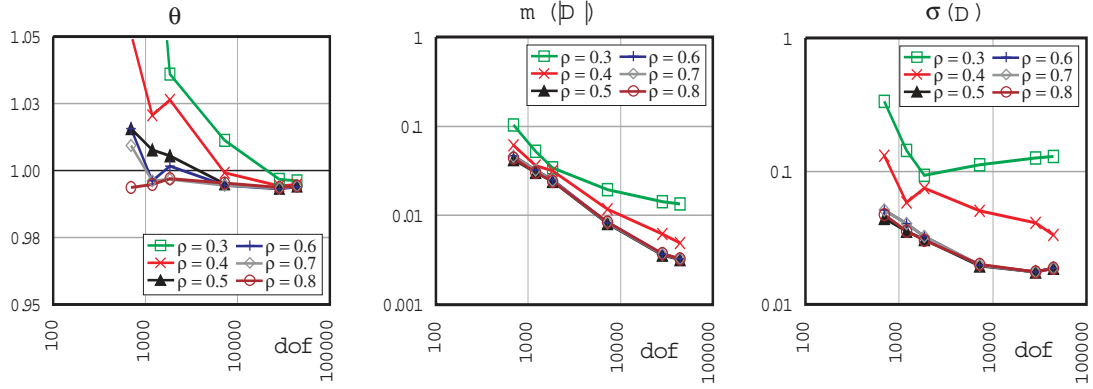
Figure 21. Mode I problem with structured meshes. Evolution of global indicators θ, $m(|D|)$ and $\sigma(D)$

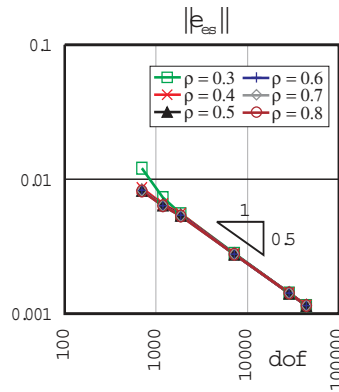for different radii ρ with a fixed enrichment radius $r_e = 0.5$.

Figure 22. Mode I problem with structured meshes. Evolution of the energy norm of the error for different

radii ρ with a fixed enrichment radius $r_e = 0.5$. Comparison with the optimal convergence rate.

The graphs show that accurate results are obtained when $\rho \geq r_e$. It can be observed

that the accuracy of the error estimator slightly increases with increasing values of ρ. In

any case we suggest the value $\rho = r_e$ as it provides accurate results and, at the same

time, restricts the use of the splitting technique to an area close to the crack tip. This

local use of the splitting technique allows for the utilization of the proposed technique

in problems with several crack tips. These figures clearly show that the results obtained

for $\rho < r_e$ are not as accurate as those obtained when $\rho \geq r_e$, especially for the coarsest

meshes. As shown in Figure 23, the reason for this is that the standard SPR technique,

based on polynomial functions, fails to adequately recover the stress field in the area

from ρ to r_e, where the XFEM solution is being represented by an standard FE interpolation enriched with the near-tip asymptotic field.
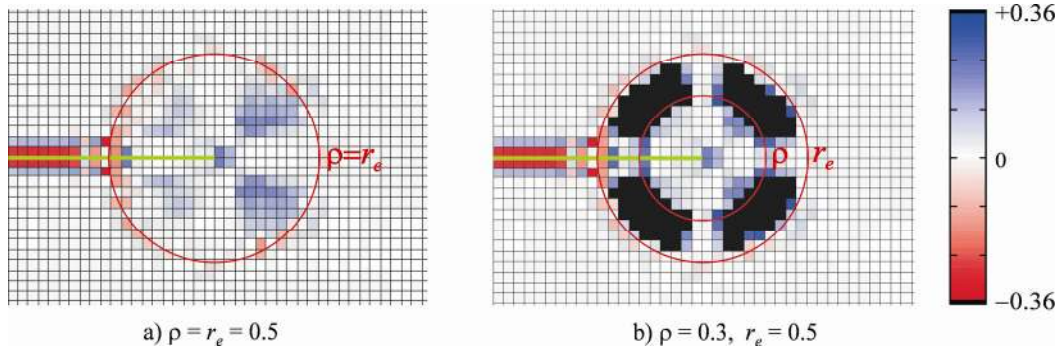

a) ρ = r_e = 0.5   b) ρ = 0.3, r_e = 0.5

Figure 23. Local effectivity index *D* in the vicinity of the singularity in a mesh of 12800 elements for the Mode I problem, with ρ = r_e and ρ < r_e .

5.7. Accuracy of recovered stress field $\boldsymbol{\sigma}^*$

The von Mises stresses $\boldsymbol{\sigma}_{vm}$ were used to evaluate the accuracy of the field $\boldsymbol{\sigma}^*$. To do this, the relative von Mises stress errors computed using the stresses from the finite element analysis, η_{vm}^h, were compared to those corresponding to the recovered stresses $\boldsymbol{\sigma}^*, \eta_{vm}^*$:

$$\eta_{vm}^h = \frac{\boldsymbol{\sigma}_{vm} - \boldsymbol{\sigma}_{vm}^h}{\boldsymbol{\sigma}_{vm}} \cdot 100 \qquad \eta_{vm}^* = \frac{\boldsymbol{\sigma}_{vm} - \boldsymbol{\sigma}_{vm}^*}{\boldsymbol{\sigma}_{vm}} \cdot 100 \qquad (24)$$

The values of η_{vm}^h and η_{vm}^* for the mode I problem were evaluated for the structured mesh number 4 (see Figure 10) on the paths shown in Figure 24. Due to the symmetry of the problem, only the upper part of these paths were considered, i.e. angles in (0,π); the values of η_{vm}^h and η_{vm}^* have been evaluated on the Gauss points closest to 36 points uniformly distributed along these curves. Note that these paths are conveniently located into the *smooth + singular* decomposition area (*R* = 0.1), in the transition area (*R* = 0.5), and in the outer area (*R* = 0.6 and *R* = 0.9).
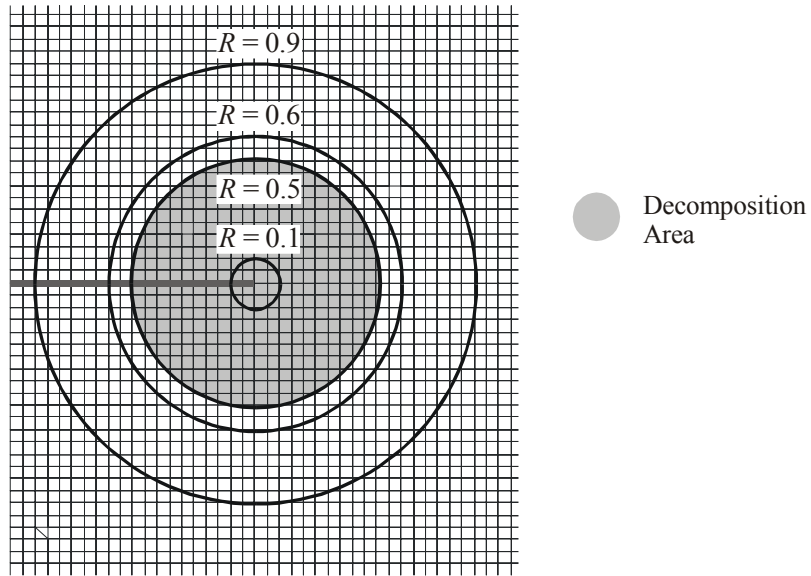
Figure 24. Stress fields for different radii around the crack tip.

The results displayed in Figure 25 show that the recovered stress field $\boldsymbol{\sigma}^*$ is considerably more accurate than the XFEM stress field $\boldsymbol{\sigma}^h$, even in the immediate vicinity of the crack tip. Therefore, in addition to providing a means of calculating accurate estimations of the energy norm discretization error, the stress field recovery method proposed in this paper can also be used to improve the accuracy of the stress fields obtained using the XFEM in LEFM problems.
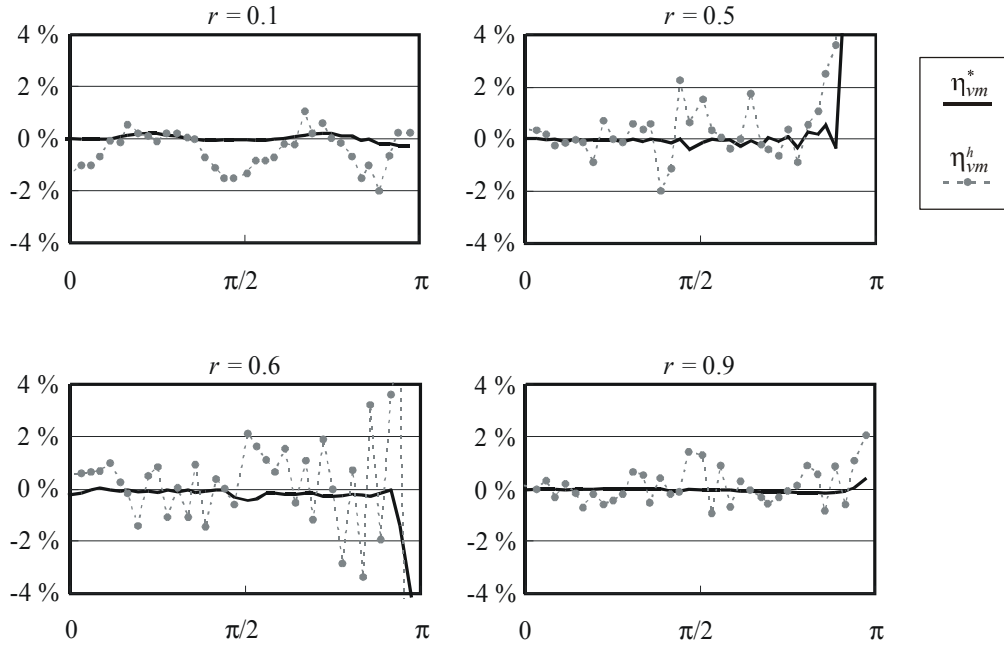
Figure 25. Relative error in von Mises stresses η_{vm} in mode I

for paths located at different radii of the crack tip.

It can be seen in both Figure 12 and Figure 18 that the error estimation for the crack faces is worse than that for the rest of the domain. The graphs in Figure 25 also show less accurate results for the area near the crack faces (angles close to π). This suggests the use of a method similar to that described in [34] in order to force the polynomials σ_p^* to fulfill the boundary conditions that need to be satisfied by the exact solution on the crack faces.

5.8. Test Problem 2: Finite plate under uniaxial tension with inclined crack

To illustrate how the method performs in cases where the exact solution is not known, a plate with an inclined crack under uniaxial traction was analyzed, see Figure 26-a. Structured meshes which ensure that the crack tip was located on the center of an element were used. In the analysis the applied load was $\sigma = 60$, and the enrichment and decomposition radii were $r_e = \rho = 0.5$. The energy norm of the estimated error for this

problem, Figure 26-b, has shown a convergence rate of 0.489, which is similar to the one of the Westergaard problem, and near to the optimal rate of 0.5, thus proving the accuracy of the technique also in this kind of problems.
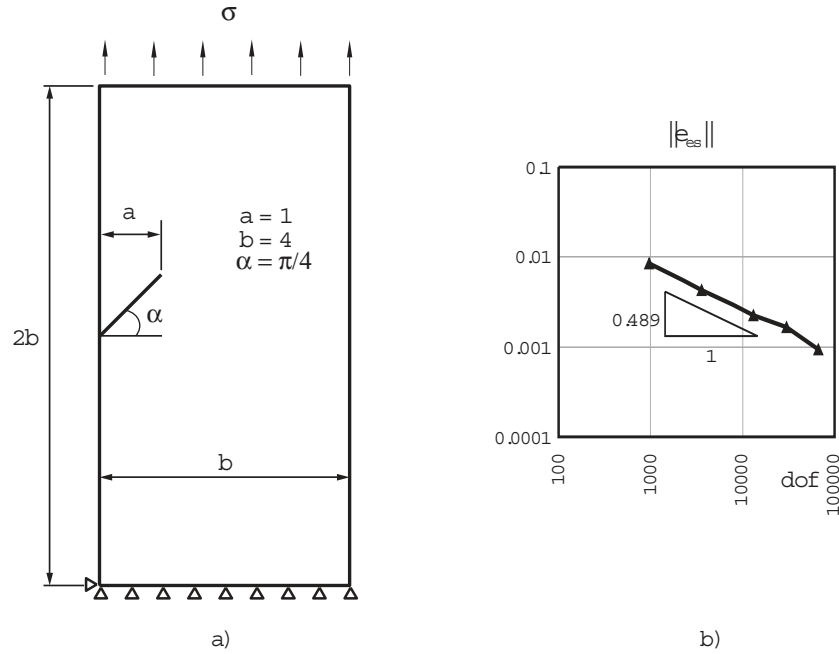

Figure 26. Inclined crack under axial tension. a) Model. b) Estimated error convergence curve

6. CONCLUSIONS

This paper has presented a recovery error estimator based on a modified version of the SPR technique that has been specifically adapted for error estimation in LEFM problems solved using the XFEM. The proposed recovery technique, called SPR$_{XFEM}$, is based on the following ideas:

- *Direct calculation of recovered stresses at integration points*. The use of the *conjoint polynomial* enhancement [23] permits the direct calculation of these stresses using adequately weighted stress interpolation polynomials calculated from different patches (and not just using their nodal values, as proposed in the standard SPR technique). This avoids the problem associated with having to

37

assign two different stress states to a single node if this is located on the crack, and the problem associated with calculating stresses in a possible node located on the crack tip.

- *Use of singular + smooth stress field decomposition.* This permits the accurate description of both the singular part of the solution based on SIF values obtained, for example, using the interaction integral, and the smooth part based on an SPR-type method.

- *Use of different stress interpolation functions at each side of the crack.* The patch formation criteria in the original SPR technique has been modified so that the stresses at each side of the crack are represented by different functions; this provides a better description of the discontinuity of the solution introduced by the crack.

The numerical results presented in this paper show that the method provides accurate estimations of the energy norm error both locally and globally, and that asymptotic exactness of the error estimator is achieved. The good quality of the error estimator is due to the accuracy of σ^*. The accuracy of σ^* was quantified by calculating the accuracy of the von Mises stresses. It was seen that the von Mises stress values calculated with σ^* were considerably more accurate than those calculated with σ^h. The SPR$_{XFEM}$ method can therefore be considered as a valid method for improving the accuracy of the stress field provided by the XFEM in LEFM problems.

ACKNOWLEDGEMENTS

REFERENCES

1. Moës N, Dolbow J, Belytschko T. A finite element method for crack growth without remeshing. *International Journal for Numerical Methods in Engineering* 1999; **46:** 131-150.
2. Sukumar N, Prévost JH. Modeling quasi-static crack growth with the extended finite element method Part I: Computer implementation. *International Journal of Solids and Structures* 2003; **40:** 7513-7537.
3. Melenk JM, Babuška I. The partition of unity finite element method: Basic theory and applications. *Computer Methods in Applied Mechanics and Engineering* 1996; **139:** 289-314.
4. Bordas S, Moran B. Enriched finite elements and level sets for damage tolerance assessment of complex structures. *Engineering Fracture Mechanics* 2006; **73:** 1176-1201.
5. Moës N, Gravouil A, Belytschko T. Non-planar 3D crack growth by the extended finite element and level sets - Part I: Mechanical model. *International Journal for Numerical Methods in Engineering* 2002; **53:** 2549-2568.
6. Sukumar N, Moës N, Moran B, Belytschko T. Extended finite element method for three-dimensional crack modelling. *International Journal for Numerical Methods in Engineering* 2000; **48:** 1549-1570.
7. Szabó BA, Babuška I. *Finite Element Analysis*. John Wiley & Sons, Inc.: New York, 1991.
8. Strouboulis T, Zhang L, Wang D, Babuška I. A posteriori error estimation for generalized finite element methods. *Computer Methods in Applied Mechanics and Engineering* 2006; **195:** 852-879.
9. Ainsworth M, Oden JT. *A Posteriori Error Estimation in Finite Element Analysis*. John Wiley & Sons: Chichester, 2000.
10. Bangerth W, Rannacher R. *Adaptive Finite Element Methods for Differential Equations*. ETH, Zürich, Birkhäuser: Basel, 2003.
11. Zienkiewicz OC, Zhu JZ. A simple error estimation and adaptive procedure for practical engineering analysis. *International Journal for Numerical Methods in Engineering* 1987; **24:** 337-357.
12. Zienkiewicz OC, Zhu JZ. The superconvergent patch recovery and *a posteriori* error estimates. Part I: The recovery technique. *International Journal for Numerical Methods in Engineering* 1992; **33:** 1331-1364.
13. Zienkiewicz OC, Zhu JZ. The superconvergent patch recovery and *a posteriori* error estimates. Part II: Error estimates and adaptivity. *International Journal for Numerical Methods in Engineering* 1992; **33:** 1365-1382.
14. Babuška I, Strouboulis T, Upadhyay CS, Gangaraj J, Copps K. Validation of *a posteriori* error estimators by numerical approach. *International Journal for Numerical Methods in Engineering* 1994; **37:** 1073-1123.
15. Babuška I, Strouboulis T, Upadhyay CS. A model study of the quality of *a posteriori* error estimators for linear elliptic problems. Error estimation in the interior of patchwise uniform grids of triangles. *Computer Methods in Applied Mechanics and Engineering* 1994; **114:** 307-378.
16. Xiao QZ, Karihaloo BL. Statically admissible stress recovery using the moving least squares technique. In *Progress in Computational Structures Technology*, Topping BHV, Mota Soares CA (eds). Saxe-Coburg Publications: Stirling, Scotland, 2004; 111-138.
17. Strouboulis T, Copps K, Babuška I. The generalized finite element method. *Computer Methods in Applied Mechanics and Engineering* 2001; **190:** 4081-4193.
18. Bordas S, Duflot M, Le P. A simple error estimator for extended finite elements. *Communications in Numerical Methods in Engineering* 2007; in press.
19. Bordas S, Duflot M. Derivative recovery and *a posteriori* error estimate for extended finite elements. *Computer Methods in Applied Mechanics and Engineering* 2007; **196:** 3381-3399.

20. Tabbara M, Blacker T, Belytschko T. Finite element derivative recovery by moving least square interpolants. *Computer Methods in Applied Mechanics and Engineering* 1994; **117:** 211-223.

21. Duflot M, Bordas S. *A posteriori* error estimation for extended finite element by an extended global recovery. *International Journal for Numerical Methods in Engineering* 2007; submitted.

22. Ródenas JJ, Giner E, Tarancón JE, González OA. A recovery error estimator for singular problems using a *singular+smooth* field splitting. *Proceedings of the Fifth International Conference on Engineering Computational Technology,* Topping B, Montero G, Montenegro R (eds). Civil-Comp Press: Stirling, Scotland, 2006.

23. Blacker T, Belytschko T. Superconvergent patch recovery with equilibrium and conjoint interpolant enhancements. *International Journal for Numerical Methods in Engineering* 1994; **37:** 517-536.

24. Belytschko T, Black T. Elastic crack growth in finite elements with minimal remeshing. *International Journal for Numerical Methods in Engineering* 1999; **45:** 601-620.

25. Stolarska M, Chopp DL, Moës N, Belytschko T. Modelling crack growth by level sets and the extended finite element method. *International Journal for Numerical Methods in Engineering* 2001; **51:** 943-960.

26. Laborde P, Pommier J, Renard Y, Salaün M. High-order extended finite element method for cracked domains. *International Journal for Numerical Methods in Engineering* 2005; **64:** 354-381.

27. Béchet E, Minnebo H, Moës N, Burgardt B. Improved implementation and robustness study of the X-FEM method for stress analysis around cracks. *International Journal for Numerical Methods in Engineering* 2005; **64:** 1033-1056.

28. Banks-Sills L. Application of the finite element method to linear elastic fracture mechanics. *Applied Mechanics Review* 1991; **44:** 447-461.

29. Li FZ, Shih CF, Needleman A. A comparison of methods for calculating energy release rates. *Engineering Fracture Mechanics* 1985; **21:** 405-421.

30. Shih C, Asaro R. Elastic-plastic analysis of cracks on bimaterial interfaces: part I- small scale yielding. *Journal of Applied Mechanics* 1988; **8:** 537-545.

31. Yau J, Wang S, Corten H. A mixed-mode crack analysis of isotropic solids using conservation laws of elasticity. *Journal of Applied Mechanics* 1980; **47:** 335-341.

32. Babuška I, Strouboulis T, Upadhyay CS. A model study of the quality of *a posteriori* error estimators for finite element solutions of linear elliptic problems, with particular reference to the behaviour near the boundary. *International Journal for Numerical Methods in Engineering* 1997; **40:** 2521-2577.

33. Boroomand B, Zienkiewicz OC. Recovery by equilibrium in patches (REP). *International Journal for Numerical Methods in Engineering* 1997; **40:** 137-164.

34. Ródenas JJ, Tur M, Fuenmayor FJ, Vercher A. Improvement of the superconvergent patch recovery technique by the use of constraint equations: the SPR-C technique. *International Journal for Numerical Methods in Engineering* 2006; **70:** 705-727.

35. Labbe P, Garon A. A robust implementation of Zienkiewicz and Zhu's local patch recovery method. *Communications in Numerical Methods in Engineering* 1995; **11:** 427-434.

36. Giner E, Fuenmayor FJ, Baeza L, Tarancón JE. Error estimation for the finite element evaluation of G_I and G_{II} in mixed-mode linear elastic fracture mechanics. *Finite Elements in Analysis and Design* 2005; **41:** 1079-1104.